Quantitative phase-contrast X-ray micro CT for visualization of mouse lymph nodes

Mirko Riedel[a,b,c], Jörg U. Hammel[c], Julian Moosmann[c], Felix Beckmann[c], Florian Schwarzenberg[d], Paul Schuetz[d], Stephan Henne[d], Clemens Wülfing[d], Madleen Busse[a,b], and Julia Herzen[a,b]

[a]Chair of Biomedical Physics, Department of Physics, School of Natural Sciences, Technical University of Munich, 85748 Garching, Germany
[b]Munich Institute of Biomedical Engineering, Technical University of Munich, 85748 Garching, Germany
[c]Institute of Materials Physics, Helmholtz-Zentrum Hereon, Max-Planck-Str. 1, 21502 Geesthacht, Germany
[d]INI-Research, Group for Interdisciplinary Neurobiology and Immunology, c/o Universität Hamburg - Zoological Institute, Martin-Luther-King-Platz 3, 20146 Hamburg, Germany

ABSTRACT

Previously, we designed a new quantitative phase-contrast setup for the microtomography experiments at the hereon beamlines P05 and P07 at PETRA III, DESY. This setup is based on Talbot array illuminators (TAI) as high visibility wavefront markers and can reach a spatial resolution level comparable to propagation-based imaging. In this work, we focus on the progress of bringing this setup into user operation. We collaborated with INI-Research to investigate the vascular system of mouse lymph nodes, exploiting the spatial resolution capabilities and using the quantitative aspect of the data to compare different sample preparation methods. We could successfully visualize and trace the blood supply of the lymph nodes, even with fine capillaries, showing the stability and performance of the setup in user application.

Keywords: phase-contrast, Talbot array illuminator, speckle-based imaging, X-ray tomography, lymph nodes

1. INTRODUCTION

Micro computed tomography (CT) setups at synchrotron facilities usually approach a resolution down to 1 µm,[1] without X-ray optics. This makes these experimental setups robust and well suited for investigating biomedical samples on a level of detail similar to conventional histology. Phase-contrast techniques are commonly used to improve the contrast for weakly absorbing soft tissues.[2] Depending on the phase-retrieval method, the spatial resolution can get deteriorated by the setup. This disadvantage is present in grating-based imaging, which is among the most popular quantitative phase-contrast methods.[3] Nevertheless, quantitative imaging methods can offer improved image quality for samples where common phase-retrieval assumptions, e.g. a homogeneous sample assumption as often used in single distance propagation based imaging, are not successfully applicable.[4]
Speckle-based imaging (SBI)[5,6] has shown in recent years its potential to be able to add to histology, by offering implicit speckle tracking techniques[7,8] or by measuring quantitative data at high-resolution.[9] By replacing the random wavefront marker, with a Talbot array illuminator (TAI),[10] we have demonstrated an improvement to SBI and have shown the capability of the technique to reach a resolution level similar to propagation-based imaging and close to the limit of the indirect detector system.[11,12] Compared to other implementations of using phase-shifting gratings,[13,14] the used TAIs show a focusing effect of 1:3 for each direction, offering a higher visibility than other configurations.
As most modern synchrotron light sources are operated as user facilities, the beamlines strive to offer a variety of

Further author information:
Mirko Riedel: E-mail: mirko.riedel@tum.de / mirko.riedel@hereon.de

methods. At the same time, these methods need to be implemented in a robust and accessible way, to minimize setup-related downtime. Due to its hardware simplicity, SBI is well suited to be run as a user experiment. The transition from a random wavefront marker to a TAI only imposes a rough fixation of the distance from TAI to the detector and thus the installation time is similar to SBI. As the phase-retrieval of most SBI methods is computationally extensive, a compute cluster is needed to process tomographic scans.
In this work, we show the transition of our setup from a preliminary development stage to a user experiment and how it can be applied in biomedical research. Together with the group of INI-Research, we investigated the vascular structure of mouse lymph nodes, showing the application of the setup for biological samples. During the course of a beamtime, several samples were scanned and afterward evaluated. We will highlight some of the scans, comparing different sample preparation procedures and their outcome.

2. MATERIALS AND METHODS

2.1 Sample Preparation

A tissue block around the inguinal lymph nodes was taken out to ensure all vascular structure inside was undamaged. The samples were fixated in 4 % paraformaldehyde in PBS for one hour before dehydration in 70 % ethanol and a subsequent series in 2-propanol. A total of six samples were prepared. For scanning them, two were transferred in liquid 70 % ethanol. Additionally, four were embedded under vacuum in Hard Plus 812 resin (EMS Diasum, Cat.Nr. 14115). In order to enhance the contrast, some of the samples were stained, using a hematein-lead complex.[15] The embedding in hard resin was preferred over other possibilities, such as paraffin, as the stain can increase the absorption to a level, where paraffin is not stable anymore.

2.2 Setup

The measurements were conducted at the micro CT setup of the imaging beamline P05 operated by hereon at PETRA III, DESY.[1,16,17] The beamline is equipped with an an undulator source and a double crystal monochromator. The samples were mounted on an air-bearing rotation stage and a lens-coupled detector with a 100 µm $CdWO_4$ scintillator and a Ximea CB500MG camera was used.
The installation TAI based setup requires the mounting of the 2D piezo stepper motor. This is attached to the camera granite structure, using a holder arm. The whole installation can be done in a few minutes. Hexagonal TAIs with a period of 10 µm, a duty cycle of DC=1/3, and a designed phase shift of $\phi = \frac{2\pi}{3}$ at a beam energy of 20 keV or 30 keV respectively were used. The scans are then recorded using multiple continuous rotation scans, with stepping the TAI in two dimensions in between the scans. The schematics of the setup are shown in Fig. 1.

The scan of the sample in liquid ethanol used 3001 projection angles over 180 degrees at an exposure time of 180 ms at a photon energy of 33 keV and a sample to detector distance of 300 mm. The scans of the hard resin embedded samples used 1501 projection angles over 180 degree at an exposure time of 120 ms at a photon energy of 20 keV and a sample to detector distance of 200 mm. All scans used 16 wavefront marker positions. The higher photon energy of the liquid embedded samples was chosen, to lower the radiation dose power on the embedding medium and to prevent gas formation.

Table 1. Scan parameters of the samples. Including the energy, number of projection angles, exposure time per projection, and the sample to detector distance.

Sample	Angular Steps	Beam Energy	Exposure time	Sample Detector Distance
Liquid embedded	3001	33 keV	180 ms	300 mm
Hard resin embedded	1501	20 keV	120 ms	200 mm

2.3 Data Processing

As a single tomographic data set using the TAI setup can reach several TB of data, transfer to an external facility for computation is not feasible for the data of a whole beamtime. Therefore a user interface to the local DESY Maxwell compute cluster was designed to run the phase-retrieval. Processing is separated into two steps:

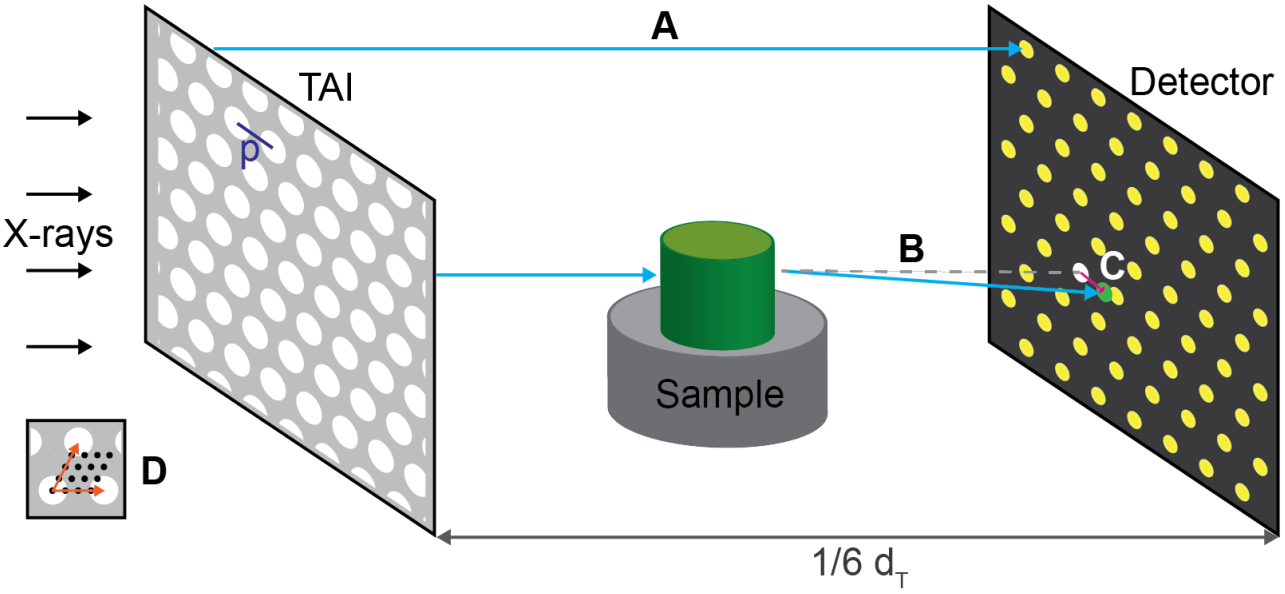

Figure 1. Schematics of the setup. The hexagonal TAI with a period p=10 µm, a duty cycle of DC=1/3, and a phase shift of $\phi = \frac{2\pi}{3}$ is illuminated by the source. In a fractional Talbot distance of 1/6 d_T, the detector is placed. The sample is mounted on the rotation stage in between. **A** marks an non refracted beamlet. If one beamlet passes the sample as shown in **B**, it is refracted from its original path (grey dashed line) an the pattern on the detector is shifted as shown by the magenta arrow in **C**. To record a full scan, multiple rotations are done, stepping the TAI in between rotations along the grating axes in fractions of a grating period, as shown in **D**. The steps are then used to determine the shift vector for each pixel using UMPA.

As the pre-processing, phase-retrieval, and integration steps are based on CPU, these steps are distributed on the cluster using multi-processing and computation on multiple nodes. The images are corrected for i.e. intensity variations, corresponding reference images are synthesized using the principal components of the flat-field images.[12,18] Phase retrieval is performed using the Unified Modulated Pattern Analysis (UMPA).[19] Afterward, the differential phase images are corrected for outliers and ramps and are integrated using a two-dimensional Fourier integration approach.[20]
The second step consists of the tomographic reconstruction. The software used for this is optimized for GPU processing, therefore a single node with large memory is needed. Before reconstruction, a ring filter was applied. Tomographic reconstruction was done using filtered back-projection and a Ram-Lak filter using the software X-Aid (Mitos GmbH, Garching, Germany).
For comparability, the reconstructed scans are converted to units of local electron density, assuming the following relationship:

$$\rho_e = \frac{k^2}{2\pi r_0} \cdot \delta, \tag{1}$$

with the wave-vector of the radiation k, the classical electron radius r_0 and the reconstructed refractive index decrement δ.[21] This allows to eliminate the energy dependence and thus makes different scans comparable.
For samples that are larger than a single field of view (FOV), it is possible to perform an off-axis scan. The scan is recorded over a full 360 deg rotation, using twice the amount of projections. Phase retrieval is performed on each projection. Afterward, opposing angles are stitched to a single image. During this, the overlap is used to correct for phase ramps of the differential projections. Phase integration is performed after the stitching as for normal scans.

2.4 Data Evaluation

The scans of the differently prepared samples were evaluated for the Contrast-to-Noise ratio (CNR) of the lymph node and its follicles. The resolution of the scans was determined, using Fourier ring correlation (FRC).[22,23]

Table 2. CNR comparison of the hard resin embedded stained and unstained node, as well as for the stained lymph node in liquid ethanol. CNR_{N-BG} denotes the CNR of the node to the embedding material background, CNR_{F-BG} of the follicle to the background, and CNR_{F-N} of the follicle to the node. The scans of the stained and unstained nodes in hard resin were measured at a photon energy of 20 keV, the scan in ethanol at an energy of 33 keV.

Sample Type	CNR_{N-BG}	CNR_{F-BG}	CNR_{F-N}
Unstained	8.66	12.02	0.52
Stained	41.42	52.61	2.77
Liquid	87.04	112.35	3.62

As resolution criteria, the full-bit and the half-bit criteria were used, equivalent to each pixel containing an information content of 1 bit or 1/2 bit respectively.
Further analysis by the group of INI-Research included a comparison to electron microscopy, immunohistochemical staining, segmentation of the vascular structure, 3D visualization, and analyzing the blood supply entry points to the node. The results are being prepared for publication.[24]

2.5 Animal Housing

The housing of the C57BL/6 mice and dissection of organs was done at the neurophysiology section of the biological department, University of Hamburg and in accordance with European Union's and local welfare guidelines (Behörde für Gesundheit und Verbraucherschutz, Hamburg, Germany; GZ G21305/591-00.33).

3. RESULTS AND DISCUSSION

3.1 Results

For the scope of this work, we focus on three of the six samples, comparing a stained sample in ethanol, a stained sample in hard resin and an unstained sample in hard resin.
The first scans were samples in liquid ethanol. An exemplary slice of a stained node can be seen in Fig. 2 **a)**. The lymph node, marked as **A**, displays a much higher electron density than the surrounding adipocytes, marked as **C**, as well as the fixating ethanol. In Fig. 2 **b)** and **c)** some follicles are shown in detail. The CNR values of the individual features are listed in Tab. 2. The adipocytes in the surrounding tissue are still filled when fixated in liquid ethanol for a short time. The electron density in the node was at 356.2(48) electrons/nm^3 and in the follicle at 380.2(45) electrons/nm^3 (yellow and orange squares). The resolution of the scan was determined, using Fourier ring correlation. The full-bit resolution was at 4.69 µm, the half-bit resolution at 4.17 µm.

As liquid embedded samples can be prone to movement during the scan, we used a second sample fixation. Embedding the samples in hard resin prohibited sample movement efficiently. In Fig. 3 images of unstained and stained lymph nodes are shown in **a)** and **b)**. The stained sample, shows a strong increase in electron density for the lymph node compared to the unstained. The contrast to the surrounding embedding material is lower, due to the higher electron density of hard resin compared to ethanol. The adipocytes are empty in the hard resin embedded samples due to the preparation process.

Comparing the effects of the stain in detail, the electron density of the unstained node is at 377.2(18) electrons/nm^3, of the follicle at 378.5(17) electrons/nm^3, whereas the stained node shows 401.6(20) electrons/nm^3 in the node and 409.1(18) electrons/nm^3 in the follicle. The corresponding CNR values are listed in Tab. 2. The spatial resolution of the unstained node, determined using FRC, was at 4.68 µm full-bit and 4.14 µm half-bit resolution. The stained node showed a resolution of 4.70 µm full-bit and 4.13 µm half-bit.

3.2 Discussion

Liquid sample fixation is a fast and simple preparation method. In the given settings, it was offering the highest CNR (cf. Tab. 2), of all features. If the sample is stable, the spatial resolution is well below 5 µm. However, as the mechanical stability in the container can be low, this preparation method is prone to sample movement. In

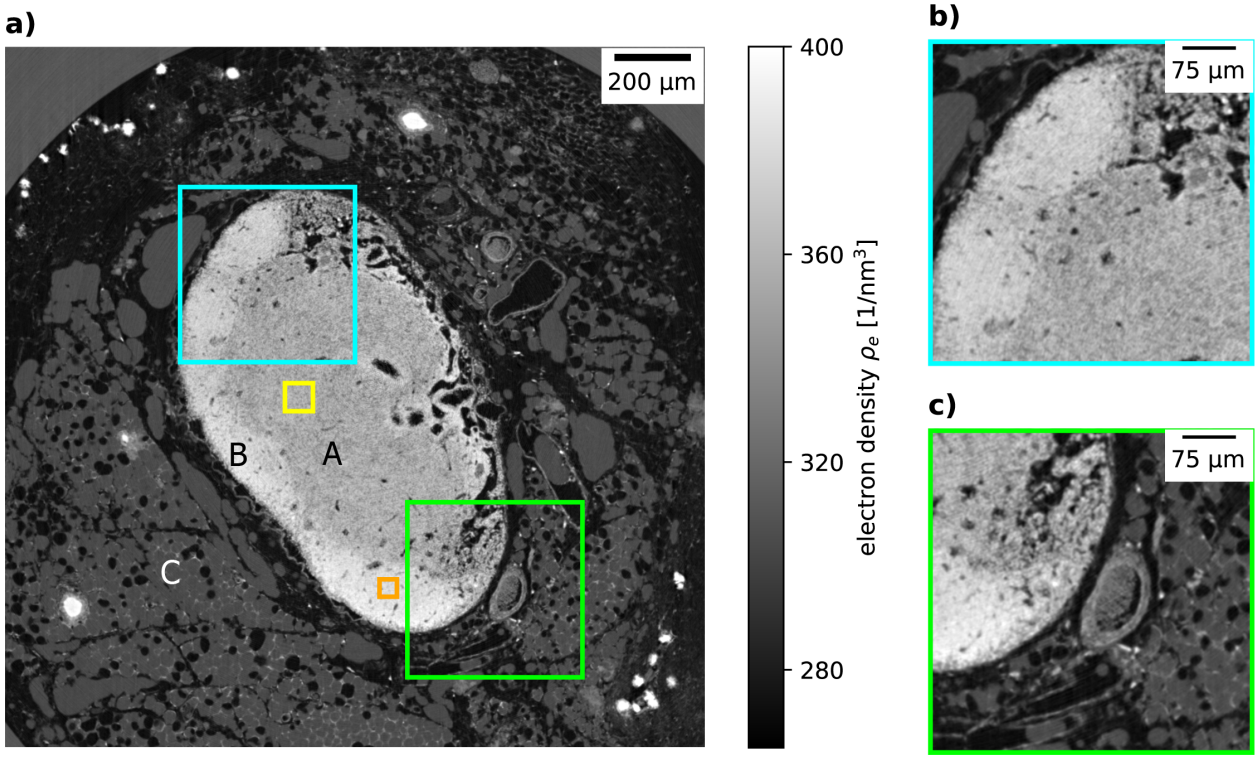

Figure 2. Scan of a stained lymph nodes in liquid ethanol, sharpened for better visual impression. In **a)** the full node is shown, zoom-ins in **b)** and **c)**. The lymph node is marked as **A**, the follicles as **B**. The surrounding tissue, mainly consisting of filled adipocytes, is marked as **C**. The fine vessels inside the node, exemplary marked in zoom-in **b** by arrows, show strong contrast. The yellow and orange colored squares mark the areas used for determining the CNR, in yellow the lymph node, in orange the follicle. The background area for the CNR is not shown.

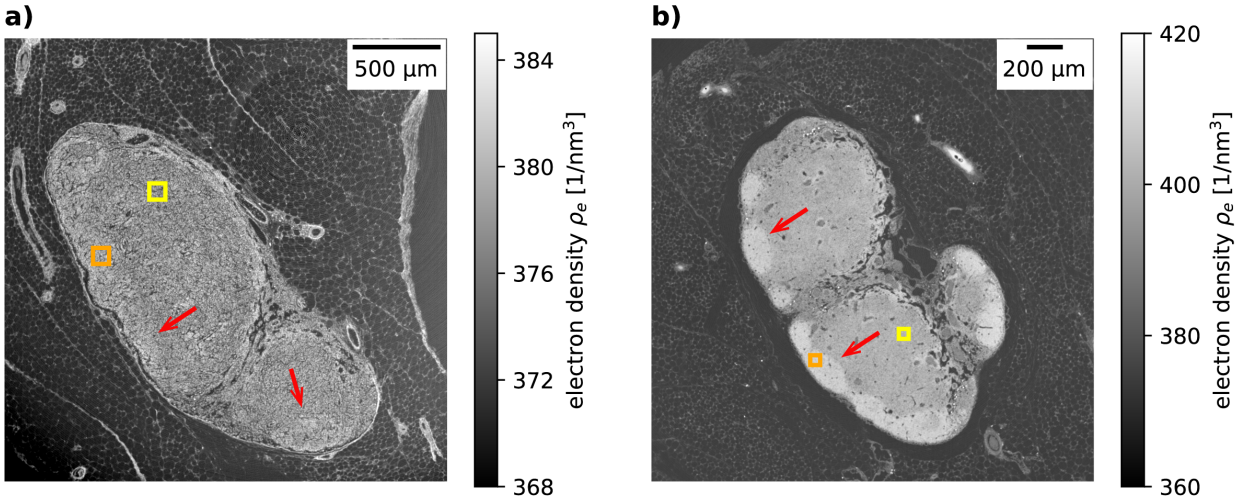

Figure 3. Comparison of an unstained lymph node in **a)**, and a stained one in **b)**. The locations of the follicles are indicated by red arrows. Due to the sample preparation, the surrounding fat cells are empty. The electron density of the stained lymph node is lower and closer to the surrounding tissue than for the stained one. The follicles are better visible stained. The colored squares mark the areas used for determining the CNR, in yellow the lymph node, in orange the follicle. The background area for the CNR is not shown.

order to prohibit sample movement, hard resin embedding offers an alternative. The preparation is more time consuming and more elaborate, but the chance of failed scans is much lower.
The CNR of hard resin embedded samples is lower compared to liquid fixation. For stained samples, all regions can be differentiated. In contrast, for unstained samples, the follicles are almost not visible, with a CNR below one. The stain induces an difference in overall electron density between stained and unstained remains at 25 electrons/nm^3 for the node and 31 electrons/nm^3 for the follicles. This shows a tendency of the stain to aggregate in the follicles.
The spatial resolution is at the same level for the hard resin embedding, as for the liquid fixation. Sample details with less than 5 µm can be identified.
To enable comparison, the scans were converted to units of local electron density. However, different setup configurations, in particular, changes in the beam energy and the sample to detector distance, influence the setup sensitivity. It drops with higher energies and shorter distances. Since the sensitivity is connected to the noise in the reconstructed data, this limits the extent to which comparison of CNR across different setup configurations is feasible.

3.3 Conclusion

This measurement series marks one of the first applications of the quantitative phase-contrast setup using TAIs at the micro CT experiment of P05 at PETRA III, DESY by an external user group. The setup was able to provide consistent results at a level of detail that enabled the analysis of the vascular system down to fine capillaries with diameters of less than 5 µm.
We tested the compatibility and compared the performance of different sample preparation methods with the setup. While all methods were able to deliver the desired results and proved compatible with further analysis, a rigid embedding is to be preferred due to the avoiding of movement artifacts. This outweighs the slightly lower CNR since all details are still well distinguishable when embedded in hard resin.
Staining the samples highlighted the node and follicles strongly. The exact behavior of the stain in the follicles is not yet described in the literature and should be investigated further.

ACKNOWLEDGMENTS

We acknowledge DESY (Hamburg, Germany), a member of the Helmholtz Association HGF, for the provision of experimental facilities. Parts of this research were carried out at PETRA III, DESY and we would like to thank Fabian Wilde for assistance in using the beamline P05, operated by the Helmholz-Zentrum Hereon. Beamtime was allocated for proposal I-20190799.
This research was supported in part by the Maxwell computational resources operated at DESY. We would like to thank Pierre Thibault and his group for providing the UMPA package.

REFERENCES

[1] Wilde, F., Ogurreck, M., Greving, I., Hammel, J. U., Beckmann, F., Hipp, A., Lottermoser, L., Khokhriakov, I., Lytaev, P., Dose, T., et al., "Micro-ct at the imaging beamline p05 at petra iii," in [*AIP conference Proceedings*], **1741**(1), 030035, AIP Publishing LLC (2016).
[2] Fitzgerald, R., "Phase-sensitive x-ray imaging," *Physics Today* **53**, 23–26 (07 2000).
[3] Bérujon, S., Wang, H., Ziegler, E., and Sawhney, K., "Shearing interferometer spatial resolution for at-wavelength hard x-ray metrology," in [*AIP Conference Proceedings*], **1466**(1), 217–222, American Institute of Physics (2012).
[4] Zanette, I., Lang, S., Rack, A., Dominietto, M., Langer, M., Pfeiffer, F., Weitkamp, T., and Müller, B., "Holotomography versus x-ray grating interferometry: A comparative study," *Applied Physics Letters* **103**(24), 244105 (2013).
[5] Bérujon, S., Ziegler, E., Cerbino, R., and Peverini, L., "Two-dimensional x-ray beam phase sensing," *Physical review letters* **108**(15), 158102 (2012).
[6] Morgan, K. S., Paganin, D. M., and Siu, K. K., "X-ray phase imaging with a paper analyzer," *Applied Physics Letters* **100**(12), 124102 (2012).

[7] Paganin, D. M., Labriet, H., Brun, E., and Berujon, S., "Single-image geometric-flow x-ray speckle tracking," *Physical Review A* **98**(5), 053813 (2018).

[8] Pavlov, K. M., Li, H. T., Paganin, D. M., Berujon, S., Rougé-Labriet, H., and Brun, E., "Single-shot x-ray speckle-based imaging of a single-material object," *Physical Review Applied* **13**(5), 054023 (2020).

[9] Zdora, M.-C., Thibault, P., Kuo, W., Fernandez, V., Deyhle, H., Vila-Comamala, J., Olbinado, M. P., Rack, A., Lackie, P. M., Katsamenis, O. L., et al., "X-ray phase tomography with near-field speckles for three-dimensional virtual histology," *Optica* **7**(9), 1221–1227 (2020).

[10] Suleski, T. J., "Generation of lohmann images from binary-phase talbot array illuminators," *Applied optics* **36**(20), 4686–4691 (1997).

[11] Gustschin, A., Riedel, M., Taphorn, K., Petrich, C., Gottwald, W., Noichl, W., Busse, M., Francis, S. E., Beckmann, F., Hammel, J. U., et al., "High-resolution and sensitivity bi-directional x-ray phase contrast imaging using 2d talbot array illuminators," *Optica* **8**(12), 1588–1595 (2021).

[12] Riedel, M., Gustschin, A., Ushakov, L., Noichl, W., Taphorn, K., Busse, M., Beckmann, F., Hammel, J., Moosmann, J., Thibault, P., and Herzen, J., "High-resolution quantitative phase-contrast x-ray imaging for biomedical samples at PETRA III," in [*Developments in X-Ray Tomography XIII*], Müller, B. and Wang, G., eds., **11840**, 123 – 131, International Society for Optics and Photonics, SPIE (2021).

[13] Morgan, K. S., Modregger, P., Irvine, S. C., Rutishauser, S., Guzenko, V. A., Stampanoni, M., and David, C., "A sensitive x-ray phase contrast technique for rapid imaging using a single phase grid analyzer," *Opt. Lett.* **38**, 4605–4608 (Nov 2013).

[14] Rizzi, J., Mercère, P., Idir, M., Silva, P. D., Vincent, G., and Primot, J., "X-ray phase contrast imaging and noise evaluation using a single phase grating interferometer," *Optics Express* **21**(14), 17340 (2013).

[15] Müller, M., Kimm, M. A., Ferstl, S., Allner, S., Achterhold, K., Herzen, J., Pfeiffer, F., and Busse, M., "Nucleus-specific x-ray stain for 3d virtual histology," *Scientific reports* **8**(1), 1–10 (2018).

[16] Greving, I., Wilde, F., Ogurreck, M., Herzen, J., Hammel, J. U., Hipp, A., Friedrich, F., Lottermoser, L., Dose, T., Burmester, H., et al., "P05 imaging beamline at petra iii: first results," in [*Developments in X-ray Tomography IX*], **9212**, 166–173, SPIE (2014).

[17] Haibel, A., Ogurreck, M., Beckmann, F., Dose, T., Wilde, F., Herzen, J., Müller, M., Schreyer, A., Nazmov, V., Simon, M., et al., "Micro-and nano-tomography at the gkss imaging beamline at petra iii," in [*Developments in X-Ray Tomography VII*], **7804**, 98–105, SPIE (2010).

[18] Van Nieuwenhove, V., De Beenhouwer, J., De Carlo, F., Mancini, L., Marone, F., and Sijbers, J., "Dynamic intensity normalization using eigen flat fields in x-ray imaging," *Opt Express* **23**(21), 27975–89 (2015).

[19] Zdora, M. C., Thibault, P., Zhou, T., Koch, F. J., Romell, J., Sala, S., Last, A., Rau, C., and Zanette, I., "X-ray phase-contrast imaging and metrology through unified modulated pattern analysis," *Phys Rev Lett* **118**(20), 203903 (2017).

[20] Kottler, C., David, C., Pfeiffer, F., and Bunk, O., "A two-directional approach for grating based differential phase contrast imaging using hard x-rays," *Optics Express* **15**(3), 1175 (2007).

[21] Als-Nielsen, J. and McMorrow, D., [*Elements of modern X-ray physics*], John Wiley & Sons (2011).

[22] Saxton, W. O. and Baumeister, W., "The correlation averaging of a regularly arranged bacterial cell envelope protein," *Journal of Microscopy* **127**(2), 127–138 (1982).

[23] van Heel, M. and Schatz, M., "Fourier shell correlation threshold criteria," *Journal of Structural Biology* **151**(3), 250–262 (2005).

[24] Schwarzenberg, F. L., Schuetz, P., Hammel, J. U., Riedel, M., Bartl, J., Bordbari, S., Frank, S.-C., Walkenfort, B., Busse, M., Herzen, J., Wuelfing, C., and Henne, S., "Three-dimensional analyzes of vascular network morphology in a murine lymph node by x-ray phase-contrast tomography with a 2d talbot array," submitted.